

# Large-scale nanophotonic phased array

Jie Sun<sup>1</sup>, Erman Timurdogan<sup>1</sup>, Ami Yaacobi<sup>1</sup>, Ehsan Shah Hosseini<sup>1</sup> & Michael R. Watts<sup>1</sup>

Electromagnetic phased arrays at radio frequencies are well known and have enabled applications ranging from communications to radar, broadcasting and astronomy<sup>1</sup>. The ability to generate arbitrary radiation patterns with large-scale phased arrays has long been pursued. Although it is extremely expensive and cumbersome to deploy large-scale radiofrequency phased arrays<sup>2</sup>, optical phased arrays have a unique advantage in that the much shorter optical wavelength holds promise for large-scale integration<sup>3</sup>. However, the short optical wavelength also imposes stringent requirements on fabrication. As a consequence, although optical phased arrays have been studied with various platforms<sup>4–8</sup> and recently with chip-scale nanophotonics<sup>9–12</sup>, all of the demonstrations so far are restricted to one-dimensional or small-scale two-dimensional arrays. Here we report the demonstration of a large-scale two-dimensional nanophotonic phased array (NPA), in which  $64 \times 64$  (4,096) optical nanoantennas are densely integrated on a silicon chip within a footprint of  $576 \mu\text{m} \times 576 \mu\text{m}$  with all of the nanoantennas precisely balanced in power and aligned in phase to generate a designed, sophisticated radiation pattern in the far field. We also show that active phase tunability can be realized in the proposed NPA by demonstrating dynamic beam steering and shaping with an  $8 \times 8$  array. This work demonstrates that a robust design, together with state-of-the-art complementary metal-oxide-semiconductor technology, allows large-scale NPAs to be implemented on compact and inexpensive nanophotonic chips. In turn, this enables arbitrary radiation pattern generation using NPAs and therefore extends the functionalities of phased arrays beyond conventional beam focusing and steering, opening up possibilities for large-scale deployment in applications such as communication, laser detection and ranging, three-dimensional holography and biomedical sciences, to name just a few.

An NPA, resembling its radiofrequency counterpart, consists of several typically identical optical antennas. Each antenna emits light of a specific amplitude and phase to form a desired far-field radiation pattern through interference of these emissions. The short wavelength of light offers potential for NPAs to greatly exceed the number of elements found in their radiofrequency counterparts, with thousands or even millions of elements in a compact, low-cost chip. By incorporating a large number of antennas, high-resolution far-field patterns can be achieved and therefore arbitrary radiation patterns can be generated by an NPA, extending the functionalities of phased arrays well beyond the conventional beam focusing and steering. However, the short optical wavelength also presents challenges in realizing coherent outputs from such large-scale NPAs because even nanoscale dimensional fluctuations affect the optical emission from the thousands of nanoantennas that need to be balanced in power and aligned in phase to form a specific far-field radiation pattern. As a consequence, all chip-based two-dimensional NPAs demonstrated so far are limited to small-scale implementations with no more than 16 antennas, and their functionalities are thereby constrained to conventional single-beam focusing and steering.

Here we report the demonstration of a large-scale, compact NPA system that is compatible with a complementary metal-oxide-semiconductor

(CMOS) process, consisting of  $64 \times 64$  optical nanoantennas on a silicon chip with all 4,096 optical nanoantennas balanced in power and aligned in phase to produce a sophisticated radiation pattern, the MIT logo, in the far field. To our knowledge, this demonstration represents the largest coherent combination of nanophotonic elements so far. It also shows that despite the short optical wavelength and corresponding length of the phase elements, the phase of the elements can be maintained, highlighting the ability to make arbitrary manipulations of the phase of an optical field within a nanophotonic chip. In addition, we demonstrate that active phase tunability can be successfully implemented in the proposed NPA structure to generate dynamic far-field patterns.

The structure of the  $64 \times 64$  NPA is illustrated schematically in Fig. 1a, and Fig. 1b shows a scanning electron micrograph (SEM) of the fabricated NPA. A laser input is coupled into the main silicon bus waveguide through an optical fibre, and then evanescently coupled into 64 row waveguides. The coupling to the row waveguides is controlled in such a way that each row waveguide obtains the same amount of power by varying the length of the directional coupler (Supplementary Fig. 1). The optical power in each row waveguide is then similarly divided into 64 optical antenna units so that all 4,096 optical nanoantennas are uniformly excited.

Each of the 4,096 optical antenna units, or 'pixels', consists of two major functional parts (Fig. 1a, inset): a nanoantenna to efficiently deliver optical power to free space, and two optical phase delay lines to accurately adjust the phase of the light arriving at the nanoantenna (Supplementary Fig. 1). Figure 1c shows the SEM of the fabricated pixel. Ideally, the pixel size should be less than half of the free-space wavelength  $\lambda_0$  of the optical emission in both the  $x$  and  $y$  directions for the radiation to have a unique interference pattern in the far field without high-order radiation lobes<sup>13,14</sup>. It is therefore crucial to make the pixel as small as possible, so as to decrease the number of high-order interference patterns in the far field. A compact and efficient optical nanoantenna is thus demanding for the NPA system. Optical nanoantennas down to subwavelength size have previously been demonstrated<sup>15–19</sup> with metal; however, to make the material systems compatible with the CMOS process, silicon-based dielectric nanoantennas are used (Fig. 1c). The compact grating-based optical nanoantenna measures  $3.0 \mu\text{m}$  in length,  $2.8 \mu\text{m}$  in width, and  $0.22 \mu\text{m}$  in thickness, consisting of only five grating teeth. A partial etch  $0.11 \mu\text{m}$  in depth is applied to the first grating groove, to break the up-down symmetry of the nanoantenna for more upward emission<sup>20</sup>. Figure 2a shows the simulated near-field emission pattern from a three-dimensional finite-difference time-domain simulation, in which 51% of the optical power emits upwards while only 30% emits downwards at  $\lambda_0 = 1.55 \mu\text{m}$ . Figure 2b illustrates the calculated far-field pattern of the optical nanoantenna, using the near-to-far-field transformation<sup>21</sup>. The emission is not vertical because the grating period is slightly detuned from that of a second-order grating that would emit vertically, to suppress the resonant back-reflections; otherwise, significant reflection would interfere with the light propagation in the phased array. The emission from the nanoantenna is also broadband, with a bandwidth extending across hundreds of nanometres in wavelength, an inherent

<sup>1</sup>Research Laboratory of Electronics, Massachusetts Institute of Technology, Cambridge, Massachusetts 02139, USA.

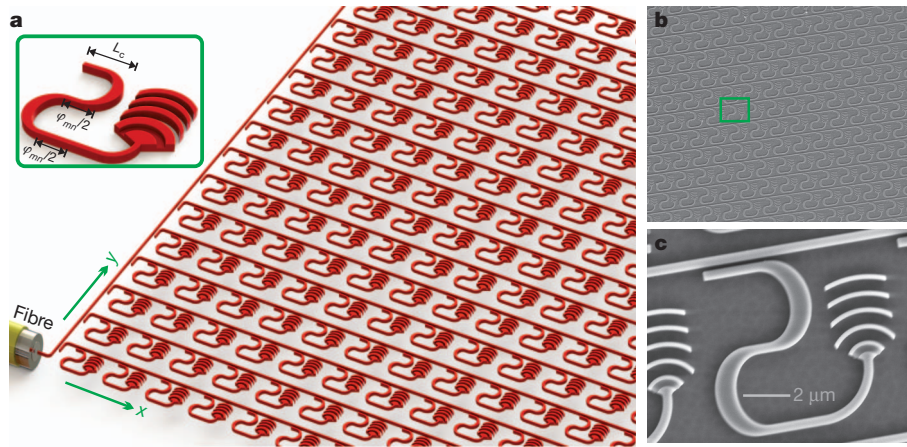


**Figure 1 | The NPA system.** **a**, Schematic illustration of a  $64 \times 64$  NPA system. Laser input from an optical fibre is delivered equally to each of the 4,096 nanoantennas through silicon waveguides. The inset shows a diagram of a close-up view of one antenna unit cell ( $m, n$ ), or 'pixel'. The coupling efficiency is varied by the length of the directional coupler  $L_c$ , and the emitting phase is controlled by two segments of optical delay lines to achieve a desired phase

delay of  $\varphi_{mn}$ . **b**, SEM of part of the  $64 \times 64$  NPA system fabricated at a CMOS foundry. **c**, A close-up SEM of one pixel of the NPA system, indicated by the green rectangle in **b**. The pixel size is  $9 \mu\text{m} \times 9 \mu\text{m}$ , with a compact grating as an optical nanoantenna, where the first groove of the grating is partly etched to enhance the upward emission. The emitted phase of each pixel is adjusted by the length of the optical delay line within the pixel.

characteristic of the short length of the grating (see also Supplementary Fig. 2).

As mentioned above, the ability to integrate a large number of pixels in the NPA within a small footprint opens up the possibility of using NPA to generate arbitrary, sophisticated far-field radiation patterns. The far-field radiation field  $E(\theta, \phi)$  of the phased array is calculated as the far field of an individual nanoantenna  $S(\theta, \phi)$  (Fig. 2b), multiplied by the array factor  $F_a(\theta, \phi)$ <sup>22</sup>

$$E(\theta, \phi) = S(\theta, \phi) \times F_a(\theta, \phi) \quad (1)$$

where the array factor is a system factor that is related to the phase of optical emission from all the pixels.  $\theta$  and  $\phi$  are the far-field azimuth angle and polar angle, respectively. By assigning the optical phase  $\varphi_{mn}$  of each pixel (where  $m$  and  $n$  are the pixel indices) in the NPA, the desired radiation pattern  $E(\theta, \phi)$  can be achieved. The phase  $\varphi_{mn}$  of each pixel can be determined by antenna synthesis through the Gerchberg–Saxton algorithm<sup>23,24</sup> (Supplementary Fig. 3). The background pattern in Fig. 2c shows the simulated array factor pattern of the  $64 \times 64$  NPA at a wavelength of  $1.55 \mu\text{m}$ , designed to generate the MIT logo in the far field. The pixel pitch is chosen to be  $9 \mu\text{m}$  in both

the  $x$  and  $y$  directions, as will be used in fabrication. The pixel pitch is a multiple of the free-space half-wavelength. The designed pattern is therefore replicated in the far field, as shown by the background pattern in Fig. 2c, because the same interference conditions occur periodically in the far field to produce higher-order patterns. Equation (1) indicates that the final far-field radiation pattern of the NPA is a multiplication of the far field of the individual nanoantenna  $S(\theta, \phi)$  (Fig. 2b) and that of the array factor  $F_a(\theta, \phi)$  (background pattern in Fig. 2c), as shown in Fig. 2c. It is seen that the designed pattern is only visible in the vicinity of the zenith, owing to the directional emission of the optical nanoantenna. Figure 2d shows a close-up view of the far field radiation pattern around the zenith, where only the top rows have enough intensity to be observed.

The simulation shows that, in principle, arbitrary radiation patterns can be produced in the far field with large-scale NPAs, by controlling the emitted phase of all the pixels correctly. However, observing the short optical wavelength ( $1.55 \mu\text{m}$ ) and the high refractive index of silicon ( $n = 3.48$ ), it is almost impossible to provide every pixel exactly with the designed phase  $\varphi_{mn}$ , because slight fabrication imperfections will cause significant phase errors. As a consequence, only if the designed NPA system is highly resistant to phase errors can this large-scale NPA be fabricated reliably and function properly.

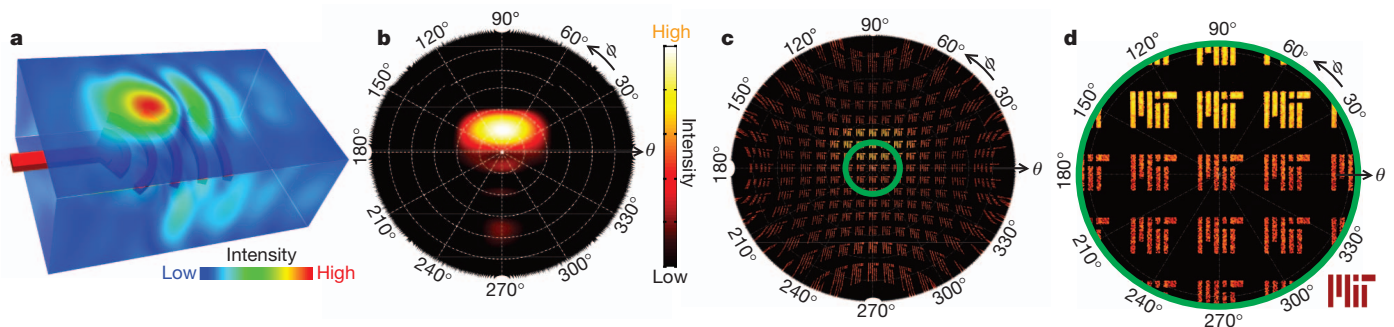


**Figure 2 | Device and system simulations.** **a**, Three-dimensional near-field emission simulation of the designed optical nanoantenna using the finite-difference time-domain method. **b**, The corresponding far-field radiation pattern of the optical nanoantenna, calculated from the near-field emission (in **a**), using the near-to-far-field transformation. **c**, The radiation pattern of the designed  $64 \times 64$  NPA system to generate the MIT logo in the far field, which is a superposition of the far field of the system's array factor (as shown in the background) and that of the nanoantenna (in **b**). The green circle in the centre

indicates the viewable region in a microscope lens (numerical aperture = 0.4) used later in the experiment (Fig. 3a). **d**, A close-up view of the viewable region of the far field displaying the MIT logo. The inset on the lower right shows the targeted MIT logo pattern. The radiation fields in **b–d** are viewed from the zenith of the far-field hemisphere, as a projection of the far-field hemisphere to the equatorial plane in the polar coordinate system  $(\theta, \phi)$ .  $\theta$  and  $\phi$  are the far-field azimuth angle and polar angle, respectively.

Fortunately, the designed large-scale NPA system is indeed highly tolerant of phase errors (Supplementary Fig. 4). This high phase-error tolerance of the designed NPA system originates from its nature as a Fourier system, in which the phase noise of the near-field emission averages out in the far field through interference of optical emissions from all the pixels. This high phase-error tolerance therefore becomes more effective with more pixels and will thus enable NPAs to scale up beyond  $64 \times 64$ , even to millions of pixels.

The robustness of the designed NPA demonstrates such a system can be fabricated reliably. The designed  $64 \times 64$  NPA was fabricated in a 300-mm CMOS foundry by 193-nm optical immersion lithography (Methods). The 4,096 pixels were accurately reproduced, as shown by the SEMs in Fig. 1b, c. A 1.55- $\mu\text{m}$  laser was coupled into the transverse electric mode of the main bus waveguide. Then the near field and far field images were captured with an infrared camera, using a setup (Fig. 3a) similar to that in ref. 25. Figure 3b shows the near-field image of the fabricated NPA system when light was coupled in, where uniform optical emission was observed across all 4,096 nanoantennas. Figure 3c shows a close-up view containing  $8 \times 8$  pixels. It is crucial for an NPA to have all the pixels emit with a desired amplitude pattern, which is uniform here, to provide an ideal interference condition in the far field. Figure 3d quantitatively analyses the uniformity of the optical emission by measuring the near-field emission intensity of each pixel with the infrared camera. A high degree of uniformity is observed. The top-left corner of the NPA is noisier, because it is close to the fibre coupling point where strong scattering occurs, but this

does not reflect non-uniformity in the array itself and can readily be addressed with a larger separation from the fibre input.

Figure 3e shows the measured far-field radiation pattern of the fabricated  $64 \times 64$  NPA. The image reveals that the designed sophisticated radiation pattern (MIT logo) is generated in the far field. The far-field image is clamped by the finite numerical aperture (0.4) of lens 1. This is also predicted by simulations, as shown by the green circle in Fig. 2c, d, where only emission with a small divergence angle from vertical can be captured. The intensity noise in the background of the far-field image comes from the light scattering caused by fibre-to-waveguide coupling. The scattered light is also responsible for the concentric fringes in the background, through the interference of the scattered light between the top and bottom surfaces of the silicon-on-insulator wafer. This noise can be removed by placing the fibre-waveguide coupler farther from the NPA system to reduce the light scattering captured by the imaging column, and a much cleaner far-field radiation pattern would be expected. Figure 3f shows the captured radiation pattern of a  $32 \times 32$  NPA on the same chip, in which less noise is observed because it is placed a little farther from the fibre coupling point; however, the far-field pattern resolution is reduced because it contains fewer pixels. The measured images agree perfectly with simulations in Fig. 2c, d, in terms of the shape of the pattern (MIT logo) and the relative intensity of all interference orders, highlighting the robustness of the NPA design and the accuracy of the fabrication. Comparing Fig. 3b with Fig. 3e, the near-field image of the NPA contains no information because it shows plain uniform

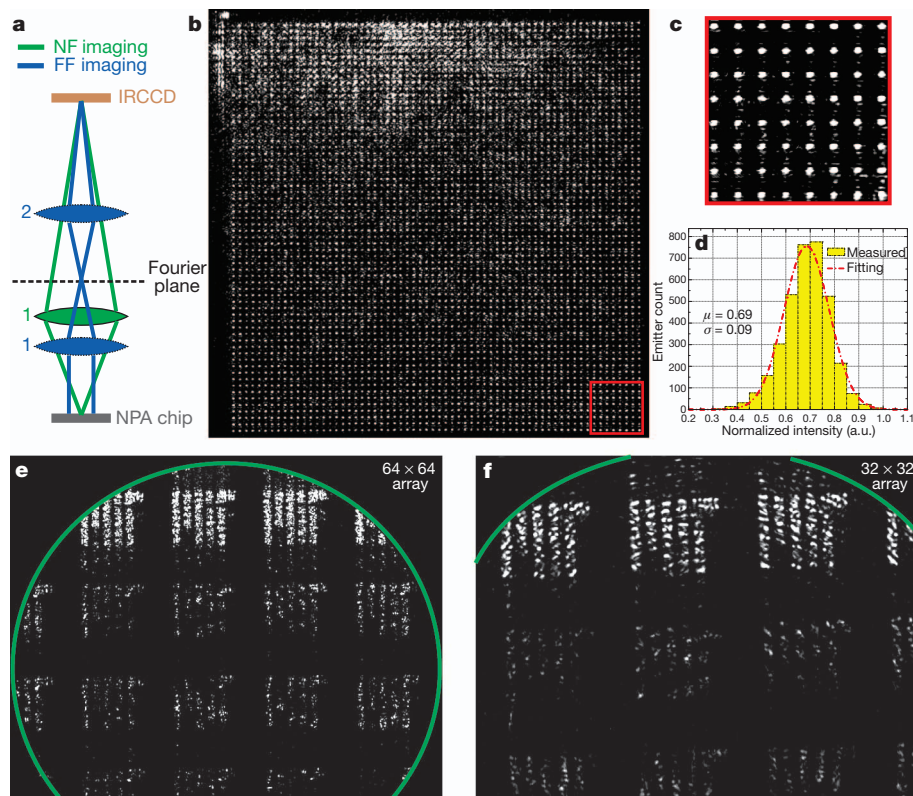


**Figure 3 | Experimental results.** **a**, A diagram of the imaging system used to observe the near field and far field. Lens 1 alone (numerical aperture = 0.40) was used to obtain the near-field (NF) image, as shown by the green rays. The far-field (FF) image, or the Fourier image, was taken by moving lens 1 down so as to form the far-field image in its back-focal plane (Fourier plane), and inserting lens 2 to project the far-field image on the infrared charge-coupled device (CCD), as shown by the blue rays. **b**, The near-field image shows uniform emission across all of the  $64 \times 64$  (4,096) nanoantennas. The input bus waveguide is located on the top left corner, causing some excess scattering noise. **c**, A close-up view of part of the near field, containing  $8 \times 8$  pixels. **d**, Measured intensity distribution of the optical emission from the pixels. The

statistics show that the standard deviation ( $\sigma$ ) of the emission intensity is 13% of the average intensity ( $\mu$ ). **e**, The far-field radiation pattern of the fabricated  $64 \times 64$  NPA system. The aperture (indicated by the green circle) corresponds to the numerical aperture (0.4) of lens 1 in **a**. The measurement accurately matched simulations in Fig. 2c, d, except for the higher background noise introduced by the light scattered from fibre-to-waveguide input coupling. **f**, The far-field radiation pattern of a  $32 \times 32$  NPA on the same chip. Less noise but lower resolution is observed. The concentric ring pattern superimposed in the image is caused by the interference of the scattered light between the top and bottom surfaces of the silicon-on-insulator wafer.

emission everywhere; however, the far field explicitly delivers the information—an image with the MIT logo. Until now, image information has generally been stored and transmitted through the intensity of the pixels; in contrast, this large-scale NPA technology opens up another dimension for imaging: the image information is now encoded in the optical phase of the pixels, much like a hologram, but generated from a single point. This demonstration, as a static phased array capable of generating truly arbitrary radiation patterns, would also find immediate applications in, for example, complex beam generation<sup>26</sup> and mode matching in optical space-division multiplexing<sup>27</sup>.

By comparison with other holographic approaches such as the metasurface antennas<sup>12</sup>, the NPA allows separate control over the phase and amplitude of light emission and on-chip single-point excitation of the nanophotonic emitters, enabling truly arbitrary holograms to be generated entirely on-chip for the first time; moreover, benefiting from the use of guided light in silicon instead of free-space light, active manipulation of the optical phase can be directly implemented to achieve dynamic far-field patterns with more flexibility and wider

applications, by converting the pixel into a thermally phase-tunable pixel in a CMOS process (Fig. 4a, inset). A portion of the silicon light path in each pixel is lightly doped with an *n*-type implant to form a resistive heater for thermo-optic phase tuning while maintaining a low loss of light propagation. Two narrow silicon leads with heavy *n*<sup>+</sup>-doping, providing electrical connections to and thermal isolation from the heater, are connected to the heater on the inner side of the adiabatic bends to minimize the loss caused by light scattering<sup>28,29</sup>. Figure 4a illustrates an active  $8 \times 8$  NPA in which each pixel has an independently tunable phase shifter; the electrical controls are connected in rows and in columns to simplify the electrical circuitry. This active  $8 \times 8$  phased array was fabricated with CMOS-processing techniques (Methods). The measured resistance is  $2.5 \text{ k}\Omega$  per heater including the two copper–silicon contacts, and a high thermal efficiency of about  $8.5 \text{ mW}$  per  $\pi$ -phase shift is achieved, benefiting from the direct heating of the silicon waveguide. By applying different voltages on each pixel, different phase combinations can be achieved in the phased array to generate different radiation patterns dynamically in the far field, as shown in Fig. 4b–f, in which five different radiation patterns

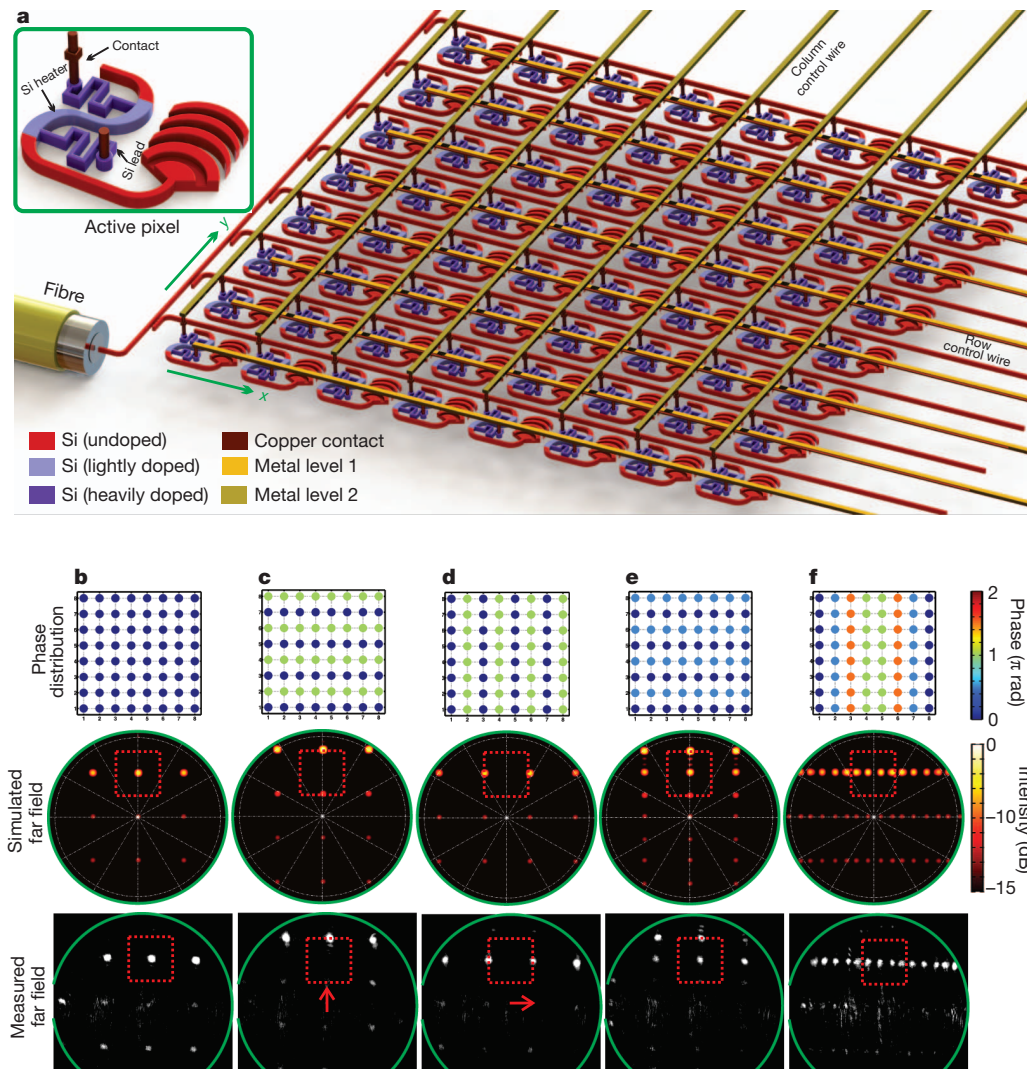


**Figure 4 | Tunable phased array.** **a**, Schematic illustration of the  $8 \times 8$  active phased array. Inset, diagram of an active pixel with the same size ( $9 \mu\text{m} \times 9 \mu\text{m}$ ) as the passive pixel in Fig. 1a. The optical phase of each pixel is continuously tuned by the thermo-optic effect through an integrated heater formed by doped silicon. **b–f**, Examples of the dynamic far-field patterns generated by the  $8 \times 8$  active phased array by applying different voltage combinations to the pixels, showing simulations and measurements. **b**, The original single-beam pattern

with no voltage on. **c, d**, The focused beam is steered by  $6^\circ$  to the edge of each interference order in the vertical (**c**) and in the horizontal (**d**). **e**, The single beam is split into two beams in the vertical direction. **f**, The single beam is split into four beams in the horizontal direction. The green circle indicates the edge of lens 1 (numerical aperture = 0.4), and the red box specifies the area of one interference order (see also the Supplementary Movie for the dynamic pattern generation).

are demonstrated using the same phased array: a standard single-beam pattern with no voltage on the array; beam-steering for about  $6^\circ$  in both the vertical direction and the horizontal direction; generation of two beams in vertical direction; and generation of four beams in the horizontal direction. Good agreement between simulation and experiment is again observed, which confirms the robustness of the proposed design as well as the accuracy of the fabrication and active thermo-optic phase tuning. The proposed active NPA structure can be immediately extended to a larger phased array (for example  $64 \times 64$ , as discussed above) with independent electrical control of each pixel with the aid of fully CMOS-controlled circuitry to access all of the pixels electrically, to project dynamic patterns in the far field with applications ranging from communications, three-dimensional holographic displays, laser detection and ranging (LADAR) and biomedical imaging to interferometry.

We have demonstrated a large-scale  $64 \times 64$  nanophotonic phased array built on a silicon photonic platform. The robustness and CMOS compatibility of the designed system enabled the successful integration of 4,096 optical nanoantennas within a chip-size footprint, probably the largest and densest silicon photonic functional system demonstrated so far, and certainly the largest coherent demonstration of silicon photonics. Optical power is uniformly distributed in the nanoantennas and is phase aligned to produce a sophisticated far-field radiation pattern, the MIT logo, as designed. The large number of nanoantennas and the embedded phase tunability enable NPAs to generate arbitrary far-field radiation patterns dynamically and, in turn, to affect new fields such as communication, LADAR, three-dimensional holography and biomedical sciences. The ability to take advantage of a state-of-the-art CMOS integration process also promises a bright future for low-cost and compact NPAs that will be important in many fields with their newly explored functionalities.

## METHODS SUMMARY

The NPAs were fabricated in a 300-mm CMOS foundry with a 65-nm technology node, using silicon-on-insulator wafers with a 0.22- $\mu\text{m}$  top silicon layer and 2  $\mu\text{m}$  buried oxide. A timed partial silicon etch (0.11  $\mu\text{m}$ ) was first performed to make the partly etched grating groove. A full silicon etch was then applied to form the waveguides and grating nanoantennas. Subsequent  $n$  and  $n^+$  dopings were implanted for active arrays, followed by standard silicidation to make copper-silicon contacts. The contacts were connected to on-chip probing pads by two metal layers for thermo-optic tuning.  $\text{SiO}_2$  with a total thickness of 3.6  $\mu\text{m}$  was used to cover the devices, with a final polishing step to make the surface planar to avoid additional phase errors due to surface corrugation.

Received 2 August; accepted 29 October 2012.

- Hansen, R. C. *Phased Array Antennas* (Wiley, 1998).
- Cherry, M. Astronomy in South Africa: the long shot. *Nature* **480**, 308–309 (2011).
- McManamon, P. F. *et al.* Optical phased array technology. *Proc. IEEE* **84**, 268–298 (1996).
- Meyer, R. A. Optical beam steering using a multichannel lithium tantalite crystal. *Appl. Opt.* **11**, 613–616 (1972).
- Resler, D. P. High-efficiency liquid-crystal optical phased array beam steering. *Opt. Lett.* **21**, 689–691 (1996).
- Ng, W. *et al.* The first demonstration of an optically steered microwave phased array antenna using true-time-delay. *IEEE J. Lightw. Technol.* **9**, 1124–1131 (1991).

- Kwong, D., Hosseini, A., Zhang, Y. & Chen, R. T.  $1 \times 12$  unequally spaced waveguide array for actively tuned optical phased array on a silicon nanomembrane. *Appl. Phys. Lett.* **99**, 051104 (2011).
- Carlson, N. W. *et al.* Electronic beam steering in monolithic grating-surface-emitting diode laser arrays. *Appl. Phys. Lett.* **53**, 2275–2277 (1988).
- Doyle, J. K. *et al.* Two-dimensional free-space beam steering with an optical phased array on silicon-on-insulator. *Opt. Express* **19**, 21595–21604 (2011).
- Van Acoleyen, K., Rogier, H. & Baets, R. Two-dimensional optical phased array antenna on silicon-on-insulator. *Opt. Express* **18**, 13655–13660 (2010).
- Van Acoleyen, K. *et al.* Off-chip beam steering with a one-dimensional optical phased array on silicon-on-insulator. *Opt. Lett.* **34**, 1477–1479 (2009).
- Yu, N. *et al.* Light propagation with phase discontinuities: generalized laws of reflection and refraction. *Science* **334**, 333–337 (2011).
- Yaacobi, A., Timurdogan, E. & Watts, M. R. Vertical emitting aperture nanoantennas. *Opt. Lett.* **37**, 1454–1456 (2012).
- Abeles, J. H. & Deri, R. J. Suppression of sidelobes in the far-field radiation patterns of optical waveguide arrays. *Appl. Phys. Lett.* **53**, 1375–1377 (1988).
- Mühschlegel, P. *et al.* Resonant optical antennas. *Science* **308**, 1607–1609 (2005).
- Schuck, P. J., Fromm, D. P., Sundaramurthy, A., Kino, G. S. & Moerner, W. E. Improving the mismatch between light and nanoscale objects with gold bowtie nanoantennas. *Phys. Rev. Lett.* **94**, 017402 (2005).
- Kosako, T., Kadoya, Y. & Hofmann, H. F. Directional control of light by a nano-optical Yagi-Uda antenna. *Nature Photon.* **4**, 312–315 (2010).
- Alù, A. & Engheta, N. Tuning the scattering response of optical nanoantennas with nanocircuit loads. *Nature Photon.* **2**, 307–310 (2008).
- Tang, L. *et al.* Nanometre-scale germanium photodetector enhanced by a near-infrared dipole antenna. *Nature Photon.* **2**, 226–229 (2008).
- Roelkens, G., Van Thourhout, D. & Baets, R. High efficiency silicon-on-insulator grating coupler based on a poly-silicon overlay. *Opt. Express* **14**, 11622–11630 (2006).
- Taflove, A. & Hagness, S. C. *Computational Electrodynamics: The Finite-Difference Time-Domain Method* 3rd edn (Artech House, 2005).
- Haupt, R. L. *Antenna Arrays: A Computational Approach* (Wiley, 2010).
- Gerchberg, R. W. & Saxton, W. O. A practical algorithm for the determination of phase from image and diffraction plane pictures. *Optik (Stuttg.)* **35**, 237–246 (1972).
- Fienu, J. R. Reconstruction of an object from the modulus of its Fourier transform. *Opt. Lett.* **3**, 27–29 (1978).
- Le Thomas, N. *et al.* Exploring light propagating in photonic crystals with Fourier optics. *J. Opt. Soc. Am. B* **24**, 2964–2971 (2007).
- Padgett, M., Courtial, J. & Allen, L. Light's orbital angular momentum. *Phys. Today* **57**, 35–40 (2004).
- Xia, C. *et al.* Supermodes for optical transmission. *Opt. Express* **19**, 16653–16664 (2011).
- DeRose, C. T. *et al.* Low power and broadband  $2 \times 2$  silicon thermo-optic switch. *Proc. Opt. Fiber Commun. Conf. OThM3* (2011).
- Watts, M. R. *et al.* Adiabatic thermo-optic Mach-Zehnder switch. *Opt. Lett.* (submitted).

Supplementary Information is available in the online version of the paper.

**Acknowledgements** We thank K. Shtyrkova and J. S. Orcutt for help with the initial measurement setup, and also APIC Corporation. This work was supported by the Defense Advanced Research Projects Agency (DARPA) of the United States under the E-PHI and SWEEPER projects, grant no. HR0011-12-2-0007. J.S. acknowledges support from DARPA POEM award HR0011-11-C-0100.

**Author Contributions** J.S. and M.R.W. conceived the idea of the project. J.S. simulated and designed the devices and the phased array system, laid out the mask and performed the experimental characterizations and analysis. E.T. helped with the NPA system simulation algorithm. A.Y. contributed to the element antenna simulation. E.H. coordinated the mask. J.S. and M.R.W. wrote the paper. M.R.W. supervised the project. All authors commented on the manuscript.

**Author Information** Reprints and permissions information is available at [www.nature.com/reprints](http://www.nature.com/reprints). The authors declare no competing financial interests. Readers are welcome to comment on the online version of the paper. Correspondence and requests for materials should be addressed to M.R.W. ([mwatts@mit.edu](mailto:mwatts@mit.edu)).